RSC *Nanoscale*

Supporting Information to

Tailoring Morphology and Structure of Tungsten Oxide Nanoparticles for Inkjet Printed Electrochromic Devices

Pawel Jerzy Wojcik*, Lidia Santos, Luis Pereira, Rodrigo Martins, Elvira Fortunato*

CENIMAT/I3N, Departamento de Ciência dos Materiais, Faculdade de Ciências e Tecnologia, FCT, Universidade Nova de Lisboa (UNL), 2829-516 Caparica, Portugal, Fax: (+351) 21 294 8558, Tel: (+351) 21 294 8562

* Corresponding authors: p.wojcik@campus.fct.unl.pt and emf@fct.unl.pt

Table of Contents

1. Strategy in metal oxide nanoparticle engineering for printed applications

To progress in the development of inkjet printed electrochromic (EC) devices, the problem has to be considered in an interdisciplinary context. This means understanding and describing the desired nanomaterial performance, as well as its technological and environmental requirements. The strategy selected in this study is based on correlation of the nanoparticles (NPs) synthesis parameters with further technological steps for ink formulation, film deposition, post-treatment and resulting film performance, as it is schematically presented in Figure 1.

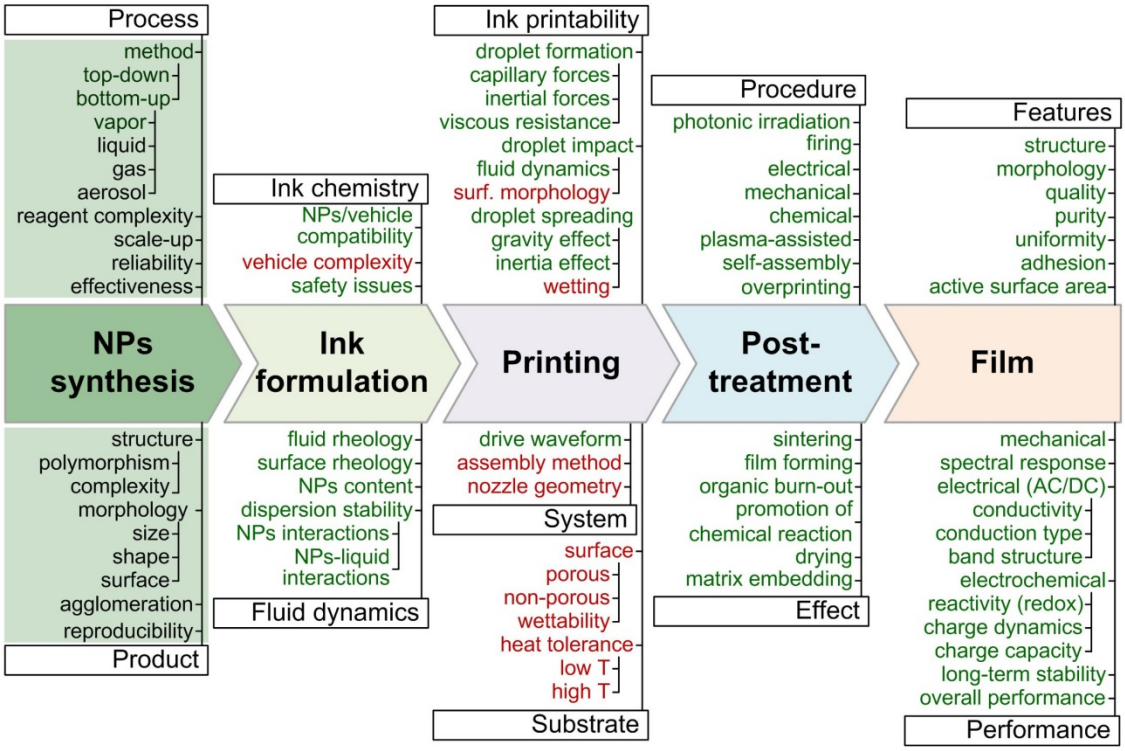

Figure S1. Simplified NPs process flow diagram for printed electrochemically active films; factors closely associated with NPs properties were colored in green, while factors considered as irrelevant were colored in red

To assure the desired electrochemical performance and processability, the criteria for NPs size, crystallinity, morphology as well as the uniformity and agglomeration mechanism are going to be established in following subsections, providing recommendations on each major technological step and determine constraints, for the application of NPs specifically in printed dual-phase EC films. However, presented here engineering rules for NPs synthesis and ink formulation have to a large extend, universal character and may be implemented to create a variety of new inkjet

printable nanostructured metal oxide (MO_X) materials for chromic, photovoltaic, photocatalytic and power storage applications.

2. Hydrothermal synthesis details

The hydrothermal synthesis was performed using Teflon-lined stainless steel autoclave (4745 general purpose vessel, Parr) and laboratory furnace with settable temperature profile (L3/11/B170, Nabertherm) as it is presented in Figure S2. The starting material for WO_X NPs synthesis consisted of previously synthesized PTA dissolved in HCl aqueous solution just before use. Prepared solution was transferred into PTFE chamber, set inside the stainless steel autoclave and installed in the oven with temperature rising from RT up to 180 °C, ramp rate ~ 5 °C/min, for selected time of 120, 240 or 360 min.

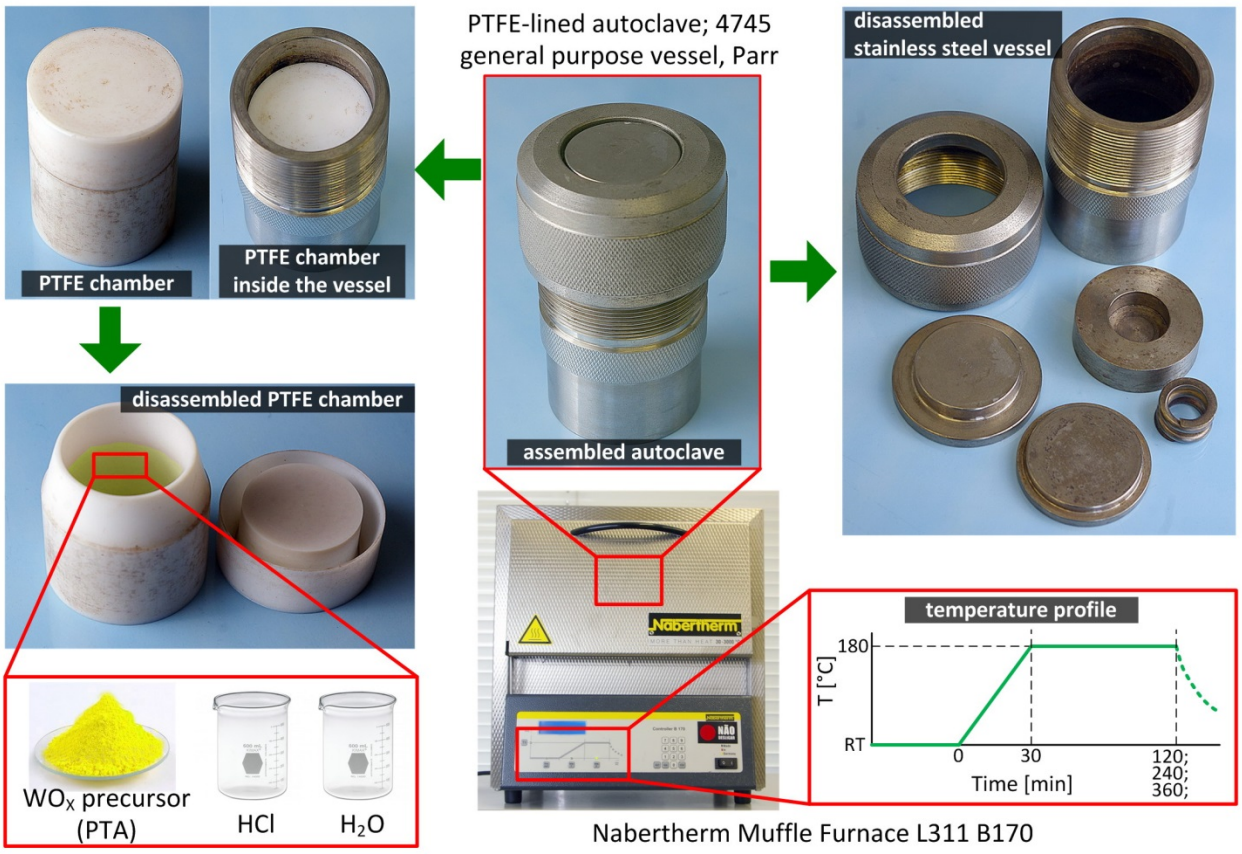

Figure S2. Hydrothermal synthesis setup

3. Hydrothermal conditions

The hydrothermal conditions for water based precursor can be approximated using well known August-Roche-Magnus empirical formula expressed by equation S1.

$$p(T) = p_0 e^{\left(\frac{17.625T}{T + 243.04}\right)} \quad \text{(S1)}$$

where: p is saturation water vapor pressure in hPa, T is temperature in °C, p_0 is saturation water pressure at T = 0 °C ($p_0 = 6.1094$ hPa). The plot of water vapor pressure in function of temperature in a range of RT-220 °C is presented in Figure S3.

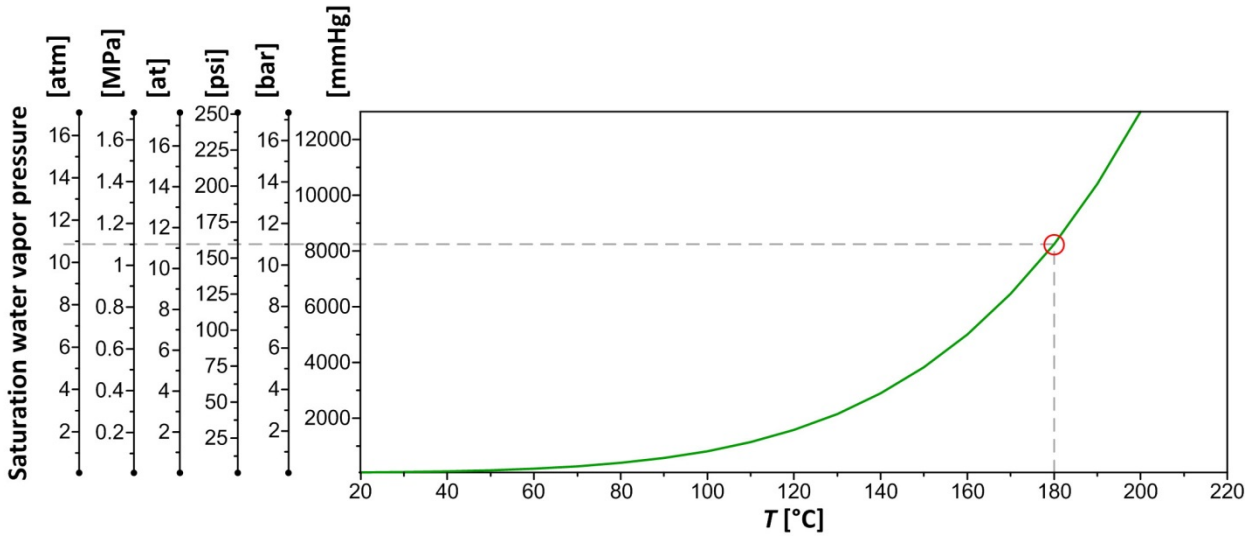

Figure S3. Saturation water vapor pressure in function of temperature as an approximation of conditions during hydrothermal synthesis

4. Inkjet printing system

A commercially available Canon PIXMA IP4500 desktop printer (Canon Virginia, Inc., Newport News, USA) with a resolution of 9600×2400 dpi was used as the printing device. This thermal-type printing unit allows deposition of the material by a digital printing process, where the ink/material is ejected directly onto a substrate from 1536 nozzles (Magenta or Cyan channel) driven by an electronic signal. The fabrication of the active layer by inkjet printing was performed at room temperature and atmospheric pressure. Necessary modifications have been carried on according to the instruction presented in Figure S4.

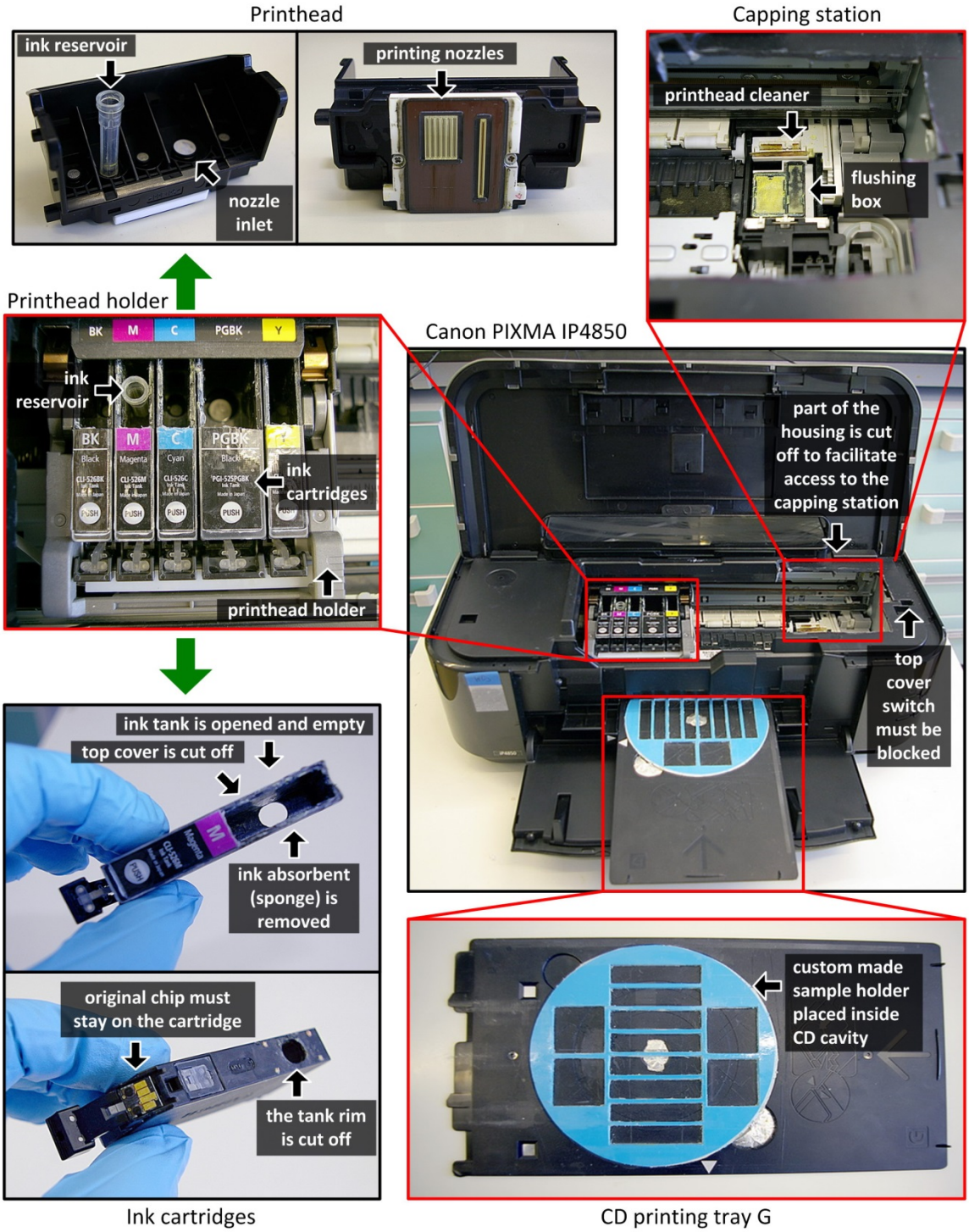

Figure S4. Modifications applied to Canon PIXMA IP4850 desktop printer; presented instruction is also valid for Canon PIXMA IP4500 used in present studies as inkjet printing system for EC film deposition.

The selection of inkjet printing system for experiments was dictated by the printer functionality, which should satisfy several requirements. Firstly, the printer enables printing on CDs using dedicated CD tray. Secondly, cartridges are not integrated with the printhead. Canon PIXMA desktop printers compatible with CD printing were found to be the most suitable for this task. Full tests were performed with models Canon PIXMA MP600 (tray F), IP4500 (tray F) and IP4850 (tray G). However, there are many potentially useful models available which differ mainly in CD printing tray used, for example:

- tray B - IP3000, IP4000, IP5000, IP6000, IP6000D, IP8500, MP750, MP760, MP780;
- tray C - IP4200, IP5200, IP6700D, MP950;
- tray D - MP500, MP530, MP800, MP830;
- tray E - Pro9000, Pro9500;
- tray F - IP4300, IP5300, MP610, MP810, MX850, MP960, MP970;
- tray G - MG5240, MG6140, MG6150, MG8140, MG8150, IP4600, IP4680, IP4700, IP4780, IP4820, IP4840, MG8120, MG6120, MG6220, MG5320, MG5220, MG5250;
- tray J - IP7200, MG6300, MG5400.

5. Sample dimensions

Optically active *a*-WO_3/WO_X films with area of 1 cm^2 were printed in ITO PET stripes with dimensions shown in Figure S5.

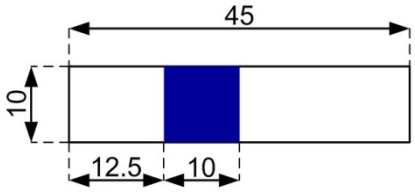

Figure S5. Sample dimensions

6. Substrate cleaning procedure

Following procedure was applied for ITO PET substrates cleaning:

a) Protection foil is removed from ITO PET surface just before cleaning procedure.
b) Both surfaces of ITO PET substrate are cleaned with lint free tissues and isopropyl alcohol.

c) First ultrasonic cleaning of substrates is performed in deionized water with 3% glass detergent (Cleaner concentrate for cuvette washing, *Fluka*) for 10 minutes at 60ºC.

d) Substrates are thoroughly rinsed with deionized water.

e) Second ultrasonic cleaning is performed in deionized water for 10 minutes at 60 ºC.

f) Substrates are thoroughly rinsed with deionized water.

g) Third ultrasonic cleaning is performed in ethanol for 5 minutes at 60 ºC.

h) Substrates are thoroughly rinsed with deionized water.

i) The last step of ultrasonic cleaning is performed in isopropyl alcohol for 5 minutes at 60 ºC.

j) If necessary, substrates can be stored in isopropyl alcohol.

k) Just before use substrates are dried by nitrogen flow.

7. Ink formulation details

The WO_X NPs loaded dispersions based on aqueous ethanol vehicle were subjected to ultrasonic treatment using ultrasonic stand mounted homogenizer (Ultrasonic Compact Hielscher UP400S) applied in ice cooled batch, as shown in Figure S6a. Sonication amplitude was applied according to the profile shown in Figure S6b.

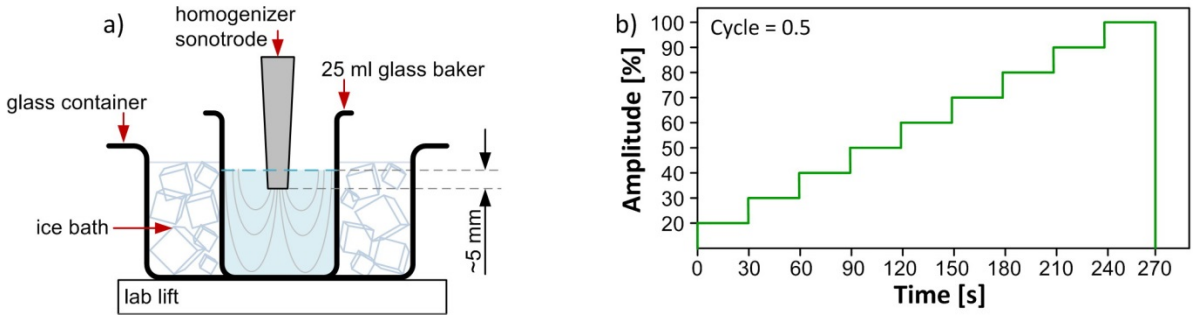

Figure S6. Ultrasonic procedure shown as a) schematic drawing and b) amplitude profile; 100 % amplitude corresponds to 400 W ultrasonic (24 kHz, automatically tuned frequency) power; cycle parameter was set as 0.5

Homogenizer was equipped with titanium sonotrode (dispersing tools) with tip diameter 3 mm, length 100 mm and male thread M10×1 designed for samples ranging from 5 up to 200 ml.

The viscosity of the ink can be easily increased to the acceptable level without substantially modifying its other properties, by addition of thickening agents. For inorganic solid/liquid mixtures, it can be a low boiling point, viscous and miscible with the vehicle organic solvent or soluble polymer, *e.g.* (for aqueous ink) polyethylene glycol (PEG) or polyvinyl alcohol (PVA). For surface tension adjustment of aqueous inks, the nonionic surfactant such as *e.g.* Triton X-100 or Triton X-45 can be added in amount of 0.1 - 0.5 wt%. In order to effectively disperse nanomaterial powder in a vehicle, breaking of NPs agglomerates and stabilization by pH modification, additions of surfactants or polymers are required. However, liquid medium complexity may significantly deteriorate electrical performance of final printed films. Therefore, in a perfect situation, NPs are dispersed in a pure water or aqueous alcoholic solution with no other organic additives, which allows for low post-treatment temperature. Moreover, it is crucial that the ink components are chemically compatible with the substrate they will be printed upon. Please note that Newtonian character of pure liquid is changing radically with the addition of NPs, due to the increased visco-elasticity of the ink.[1,2] As a consequence, the formation of the fluid drops from the nozzle is disrupted leading to the formation of satellite drops, which deteriorate pattern quality. Non-linear character of the share stress in a function of share rate affects also the droplet behavior on a substrate surface in the moment of impact (deposition, splashing or rebound) and spreading (pattern size).[3] However, changes in droplet generation, impact type and spreading dynamics are dependent rather on NPs volume fraction and agglomeration process than on their individual morphology. It is therefore more important to focus on liquid fraction of the ink and ensure its proper wettability on a surface by addition of a wetting agent, *e.g.* (for aqueous ink) ethylene glycol butyl ether (EGBE), or to carry out a surface pretreatment of a substrate.

8. Optical measurements set-up

The optical responses of the films were measured in two-electrode configuration cell shown in Figure S7. *Working electrode* consists of ITO PET substrates coated with optically active *a*-WO_3/WO_X electrode, while platinum wire serves as *reference* and *counter* electrode. Both electrodes are immersed in liquid/gel electrolyte.

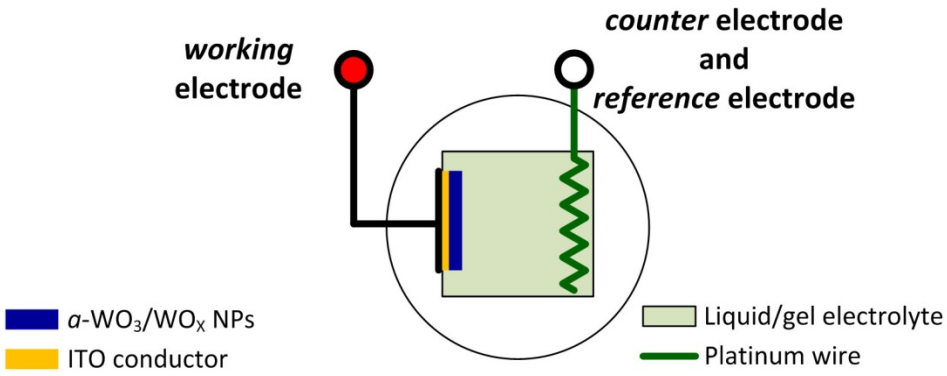

Figure S7. Configuration of opto-electrochemical cell in optical measurements

A sufficient degree of agreement between successive *measurements* (measurement r*eproducibility*) is assured by custom-made PTFE cell and acrylic cuvette holder. Proper sample installation and corresponding protocol are presented in Figure S8. All optical measurements are performed in reference to dummy cell which is assembled the same way, but does not contain optically active film.

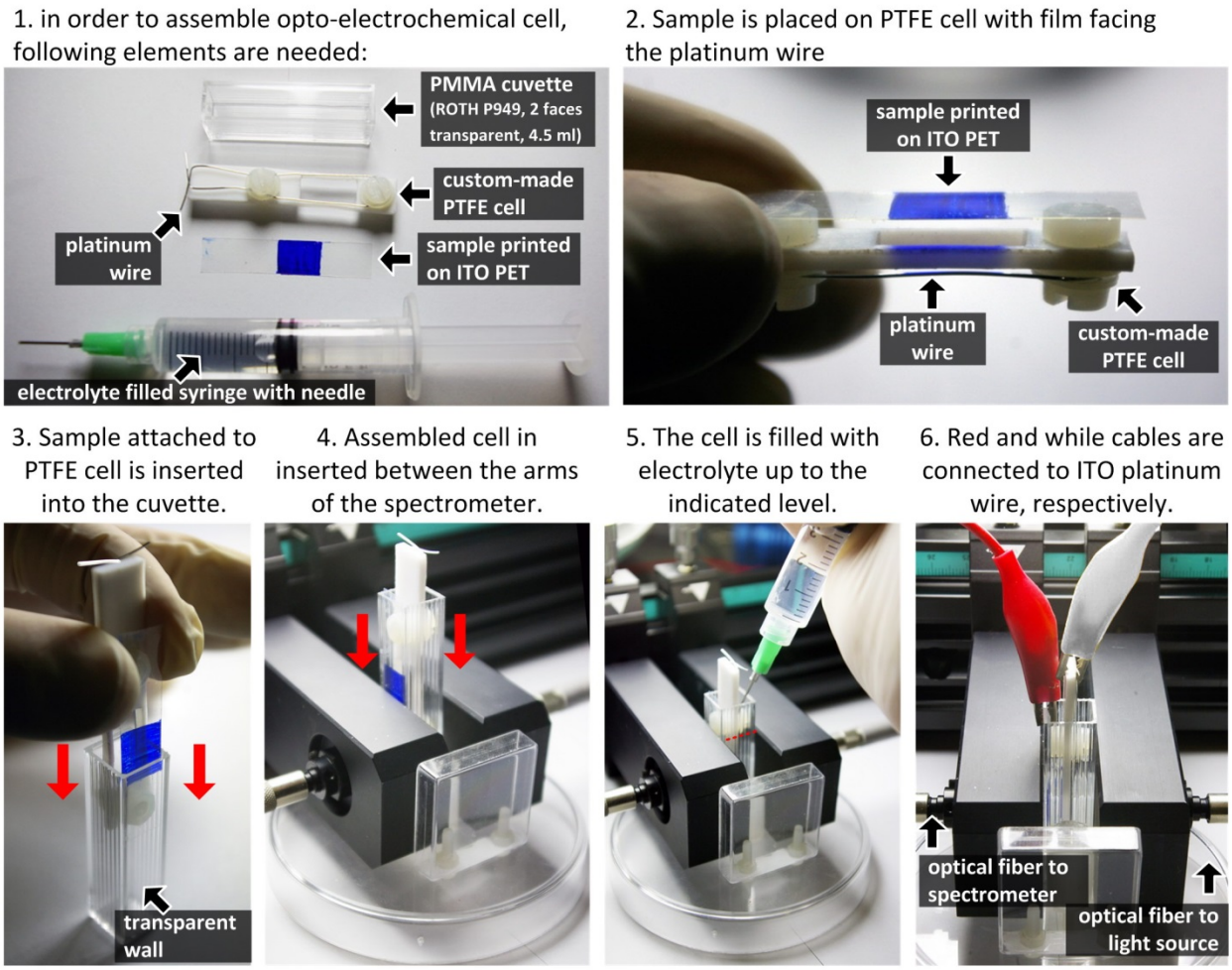

Figure S8. Protocol for sample installation inside custom made PTFE cell and its integration with spectrometer using custom-made acrylic cuvette holder.

The optically active area of the device changes from dark blue color to transparent when stimulated by an electric current applied to electrodes. As two opposite walls of the cuvette are transparent, and PTFE cell does not cover the optical path, coloration and bleaching can be seen clearly through it, which enables integration of the cell with spectrometer.

Optical measurements were performed using spectrometer set-up shown in Figure S9. Main elements of this system are: UV-Vis spectrometer (HR4000 High-Resolution Spectrometer, Ocean Optics), light source (HL-2000-FHSA Halogen Light Source, Mikropack), power supply (High Current Source Measure Unit, KEITHLEY 238) and optical fibers (QP600-2-SR/BX, type – SR, core diameter - 600 μm, connector – QSMA, jacketing – BX).

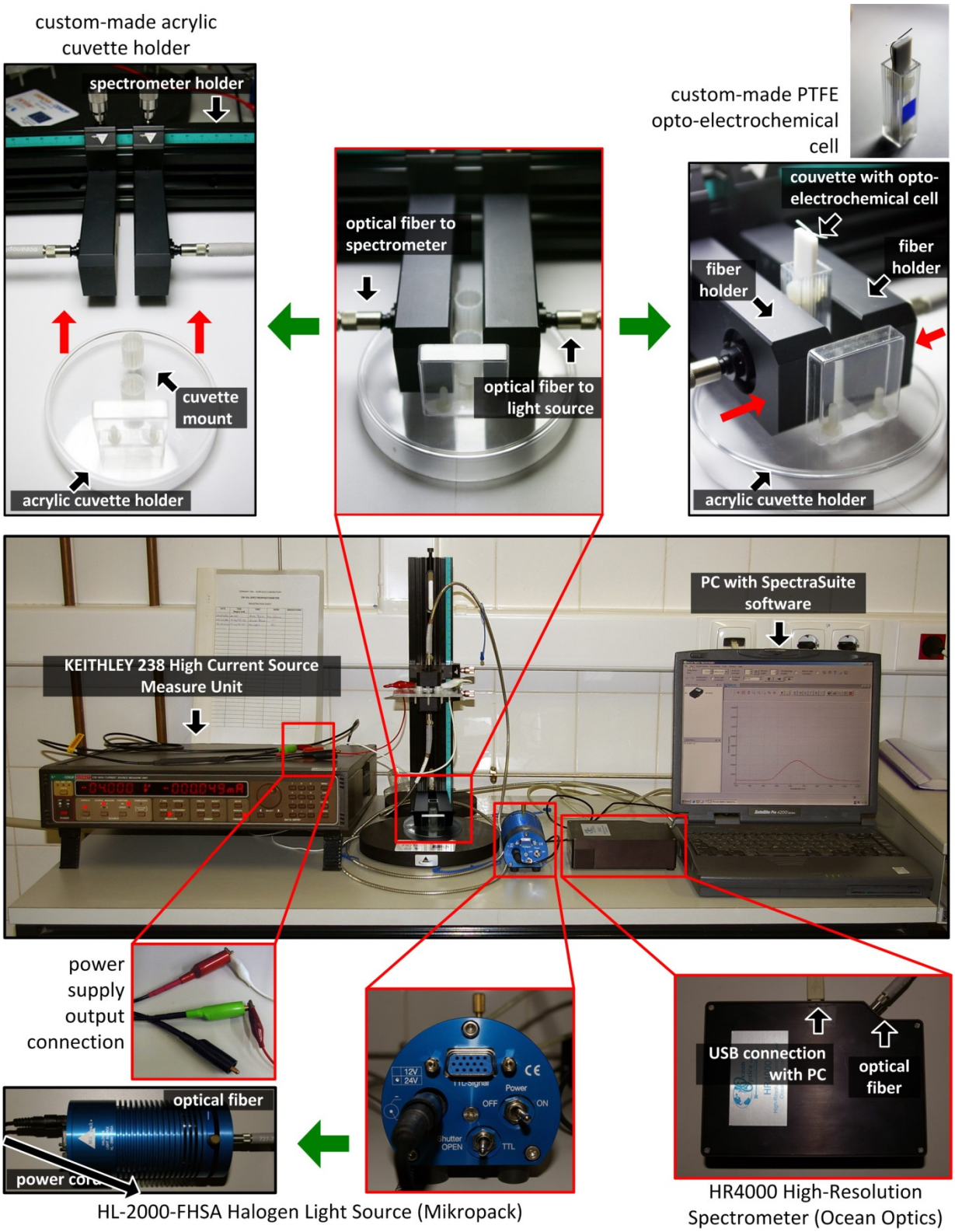

Figure S9. Optical measurement system set-up

9. Definitions of parameters

Optical measurements are based on chronoabsorptometry (CA) technique which is a square-wave potential step method coupled with optical spectroscopy used for analysis of switching kinetics and contrast of the film. The EC testing was processed within an appropriate voltage range (-2 V to 2 V), so as to avoid electrolyte oxidation and (eventual) ITO reduction. The main output from CA measurements is the change in optical density (ΔOD), which indicates how much the transmittance of the EC layer is reduced during the coloring process (or increased during bleaching) for various levels of operational voltage. A linear stair pulse wave form shown in Figure S10a was used to induce EC action, and the optical response recorded for λ = 800 nm was analyzed according to Figure S10b.

The change in optical density is calculated using equation S2.

$$\Delta OD = \log_{10}\left(\frac{T(t_n,\lambda)}{T(t_{n+1},\lambda)}\right) \quad \text{(S2)}$$

where: $T(t_n,\lambda)$ and $T(t_{n+1},\lambda)$ are transmittances of the films at λ = 800 nm before (t_n) and after (t_{n+1}) coloration process, respectively for each level of operational voltage (see also Figure S10b).

The impact of WO_X NPs on reversibility of printed dual-phase EC films is measured as ΔT_{SS} which represents so called site saturation effect.[4] The ΔT_{SS} is defined according to equation S3 as the difference in average transmittance ($T(t_0,\lambda)$, λ = 800 nm) of the film bleached by negative voltage to its bleached value after coloration for particular operating voltage (U) (see also Figure S11). The ΔT_{SS} is equal to 0 for fully reversible optical effect.

$$\Delta T_{SS} = T(t_0,\lambda) - T(t_m,\lambda, U) \quad \text{(S3)}$$

Site saturation effect is quantified based on the CA results with linear stair pulse wave form shown in Figure S10a used to induce EC action.

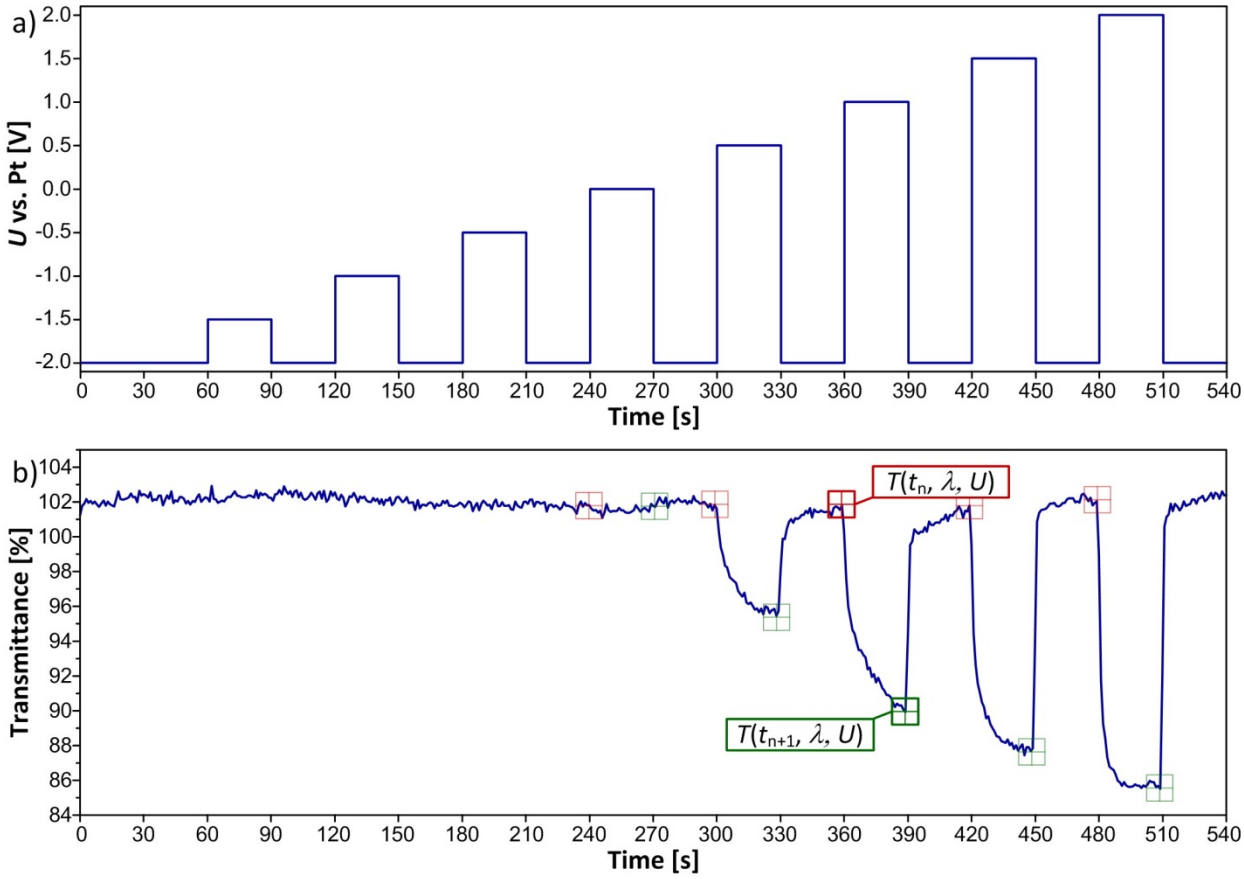

Figure S10. Determination of $^{\Delta OD}$ as a function of operational voltage based on chronoabsorptometry technique in which a) linear stair pulse wave form is supplied to the film and its b) optical response at λ = 800 nm is recorded showing change in transmittance depending of the level of supplied voltage; an example shows optical response of a *a*-WO_3/WO_X film based on a products of 4 hours long synthesis performed from the PTA precursor dissolved in 0.3 M HCl (*ortho*-$WO_3 \cdot 0.33H_2O$ nanorods).

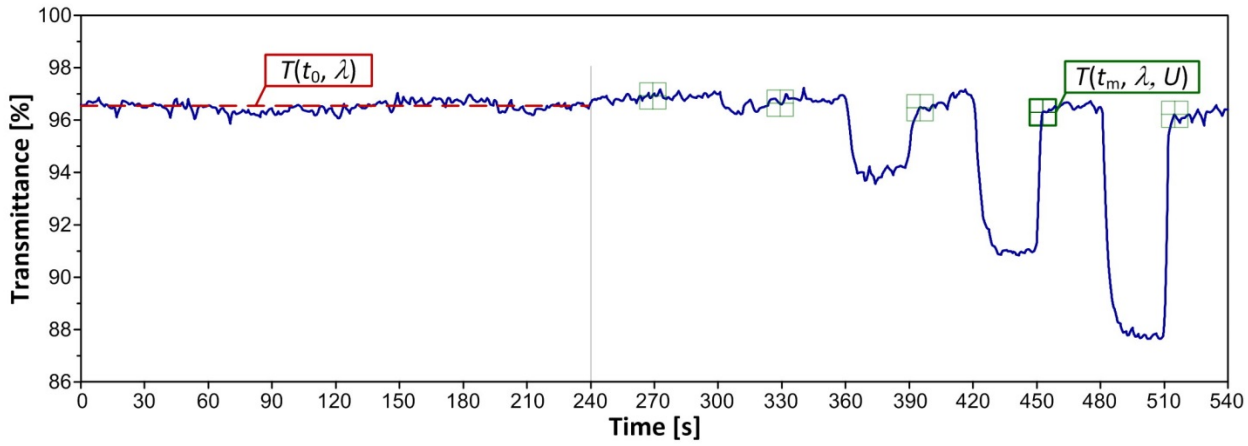

Figure S11. Determination of $^{\Delta T_{SS}}$ as a function of operational voltage based on recorded optical response at λ = 800 nm; an example shows optical response of *a*-WO_3 film with no NPs incorporated.

Data obtained from CA measurements in which square wave potential (see Figure S12a) is applied, enables estimation of the switching time for coloring and bleaching process according to Figure S12b.

The coloration time (τ_{col}) is defined as the time required for an EC device to change from its bleached to colored state. In present studies the coloration time is defined as the requisite time for reduction of the device's transmittance to 80% of the final reduction according to equation S4 (see also Figure S12b).

$$\tau_{col} = f^{-1}\left(T(t_2, \lambda) + 0.2\left(T(t_1, \lambda) - T(t_2, \lambda)\right)\right) - t_1 \qquad \text{(S4)}$$

The bleaching time (τ_{bl}) is defined as the time required for an EC device to change from its colored to bleached state. In these studies the bleaching time is defined as the requisite time for change of the device's transmittance to 80% of the final bleach level, according to equation S5 (see also Figure S12b).

$$\tau_{bl} = f^{-1}\left(T(t'_2, \lambda) - 0.2\left(T(t'_2, \lambda) - T(t'_1, \lambda)\right)\right) - t'_1 \qquad \text{(S5)}$$

The values of τ_{col} and τ_{bl} were determined as average values obtained from 5 consecutive cycles.

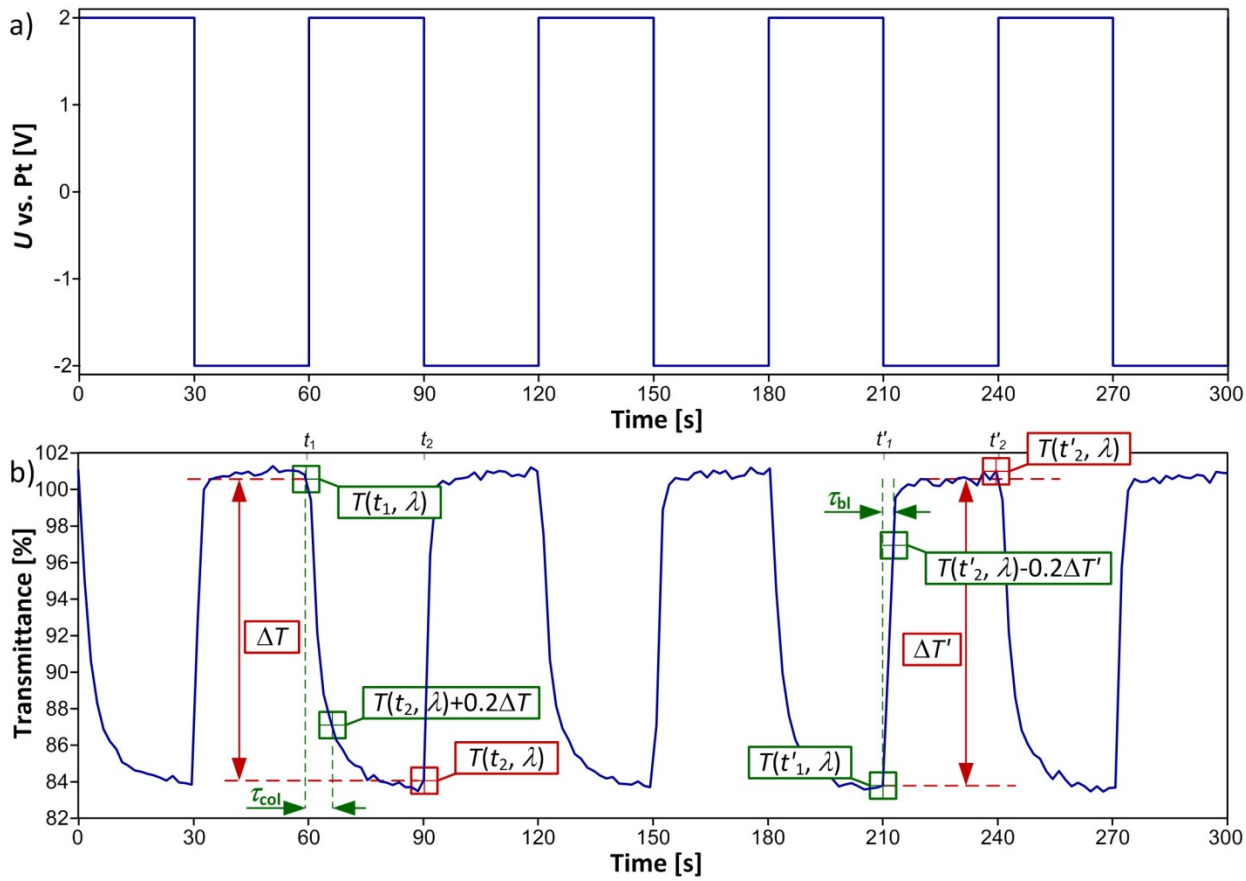

Figure S12. Determination of coloration and bleaching time based on chronoabsorptometry technique in which a) square wave form is supplied to the film and its b) optical response at λ = 800 nm is recorded showing change in transmittance; an example shows optical response of a *a*-WO_3/WO_X film based on a products of 4 hours long synthesis performed from the PTA precursor dissolved in 0.3 M HCl (*ortho*-$WO_3 \cdot 0.33H_2O$ nanorods).

10. Molecular crystal model

Molecular crystal models of monoclinic tungsten oxide (*m*-WO_3) and orthorhombic tungsten oxide hydrate (*ortho*-$WO_3 \cdot 0.33H_2O$) were simulated using CrystalMaker® for Windows ver. 2.3.0. Crystal of *m*-WO_3 presented in Figure S13a was simulated according to ICSD: 98-009-1587 with following cell parameters and crystal structure (X, Y, Z): space group P 1 21/c 1; space group number 14; a = 7.2973 Å; b = 7.5390 Å; c = 10.5150 Å; alpha = 90°; beta = 133.0250°; gamma = 90°; W_1 = (0.03400, 0.47700, 0.28400); W_2 = (0.52800, 0.03700, 0.28200); O_1 = (0.21400, 0.01300, 0.49300); O_2 = (0.21600, 0.04300, 0.00800); O_3 = (0.01900, 0.24100,

0.23000); O_4 = (0.49800, 0.26200, 0.28600); O_5 = (0.72500, 0.47400, 0.21800); O_6 = (0.29400, 0.54200, 0.28900).

Crystal of *ortho*-$WO_3 \cdot 0.33H_2O$ presented in Figure S13b was simulated according to ICSD: 98-003-7822 with following cell parameters and crystal structure (X, Y, Z): space group F m m 2; space group number 42; a = 7.3450 Å; b = 12.5470 Å; c = 7.7370 Å; alpha = 90°; beta = 90°; gamma = 90°; W_1 = (0.00000; 0.00000; 0.32520); W_2 = (0.25000; 0.25000; 0.26800); O_1 = (0.00000; 0.00000; 0.57800); O_2 = (0.00000; 0.00000; 0.00000); O_3 = (0.25000; 0.25000; 0.02900); O_4 = (0.20000; 0.11200; 0.25400); O_5 = (0.00000; 0.30100; 0.22200).

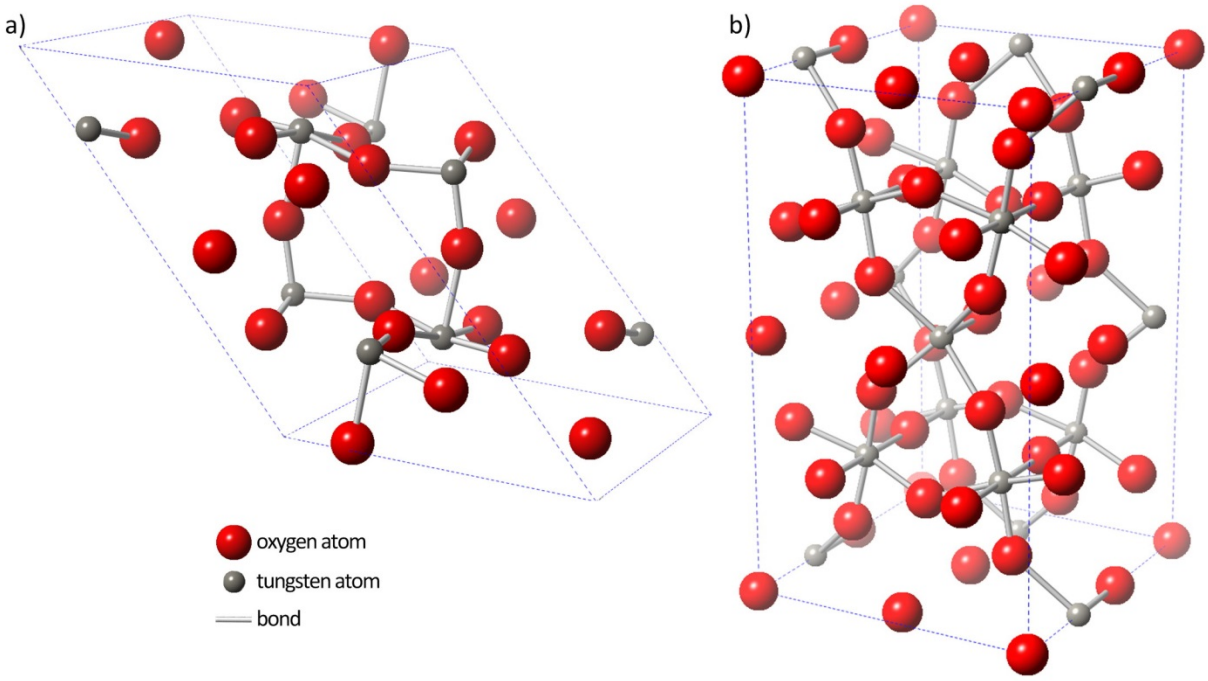

Figure S13. Models of a) *m*-WO_3 and b) *ortho*-$WO_3 \cdot 0.33H_2O$ crystals generated using CrystalMaker® software based on ICSD: 98-009-1587 and ICSD: 98-003-7822, respectively.

Models were applied to generate reference XRD patterns using CrystalDiffract® for Windows ver. 1.3.3. Resulted spectra were in full compliance with corresponding ICSD files.

11. 3D NPs Model development

3D models of monoclinic tungsten oxide (*m*-WO_3) and orthorhombic tungsten oxide hydrate (*ortho*-$WO_3 \cdot 0.33H_2O$) NPs were built using KrystalShaper software (©JCrystalSoft), version 1.3.1 according to diagram presented in Figure S14.

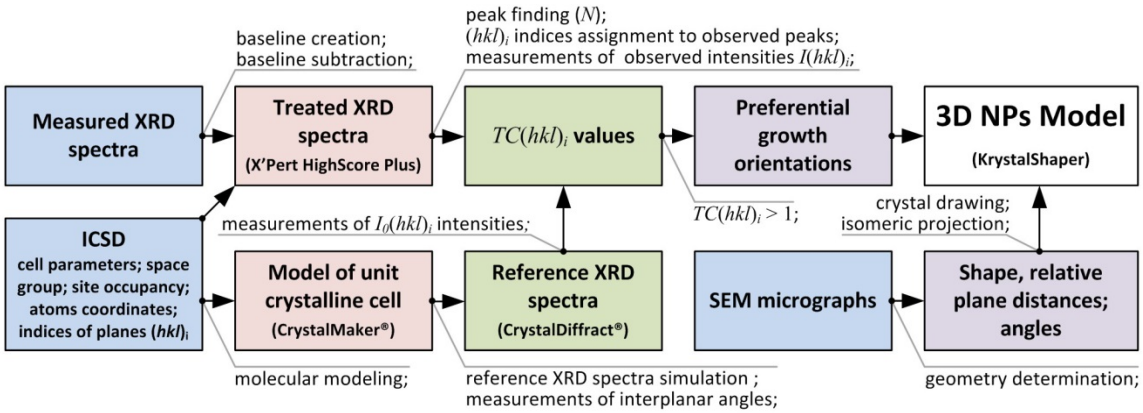

Figure S14. Schematic diagram of 3D NPs model creation process based on information obtained from the analysis of preferential growth and SEM observations.

Quantitative information concerning the preferential crystalline orientation was obtained on a basis of texture coefficient (*TC*) expressed by equation S6[5]:

$$TC(hkl)_i = \frac{\frac{I(hkl)_i}{I_0(hkl)_i}}{\frac{1}{N}\sum_n \frac{I(hkl)_n}{I_0(hkl)_n}} \quad \text{(S6)}$$

where: $I(hkl)_i$ is the observed intensity of $(hkl)_i$ plane, $I_0(hkl)_i$ is the intensity of $(hkl)_i$ reflection of a polycrystalline sample, N is the total number of reflections taken into account, and (hkl) denotes the Miller indices of the lattice planes of a given signal. TC values larger than 1 indicate a preferred orientation of the crystals/grains in the samples. By using this equation, the preferential orientation of the facets can be understood. TC$(hkl)_i$ is expected to be unity for facets which does not have preferential orientation. If TC$(hkl)_i$ is higher than unity, it is a preferentially grown facet. TC$(hkl)_i$ values of facets of WO_X NPs taken under account are presented in Figure S15 and Figure S16.

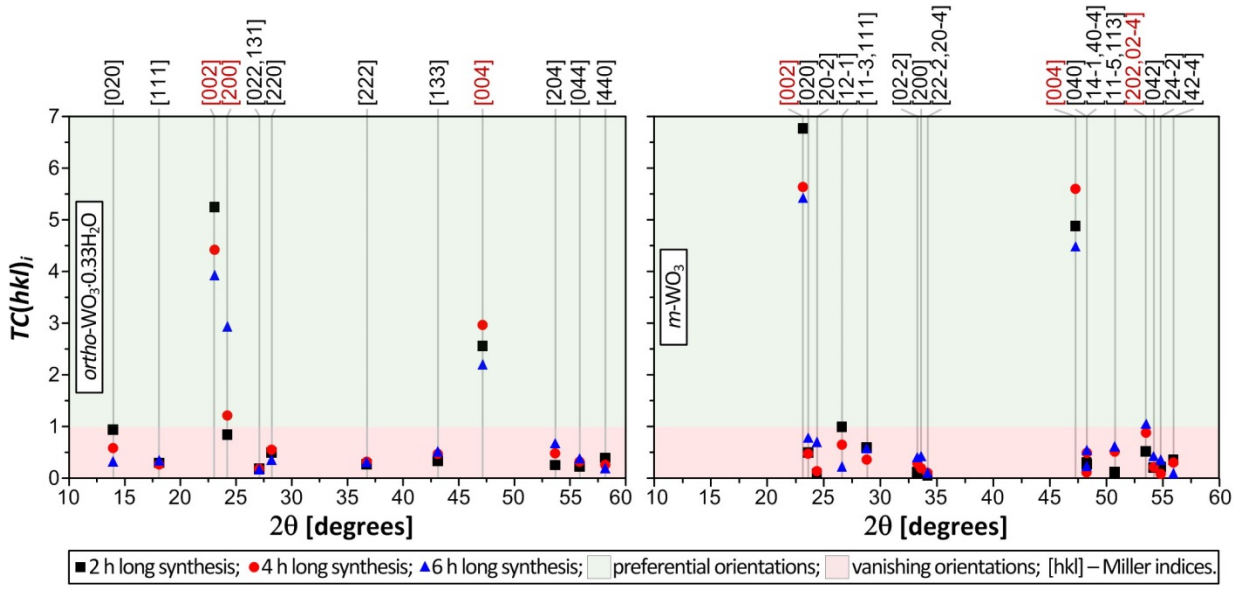

Figure S15. Texture coefficient spectra calculated for nanopowders obtained via hydrothermal syntheses performed from non-acetified precursor solution after 2 h, 4 h and 6 h; Miller indices of preferential orientations were highlighted by red color.

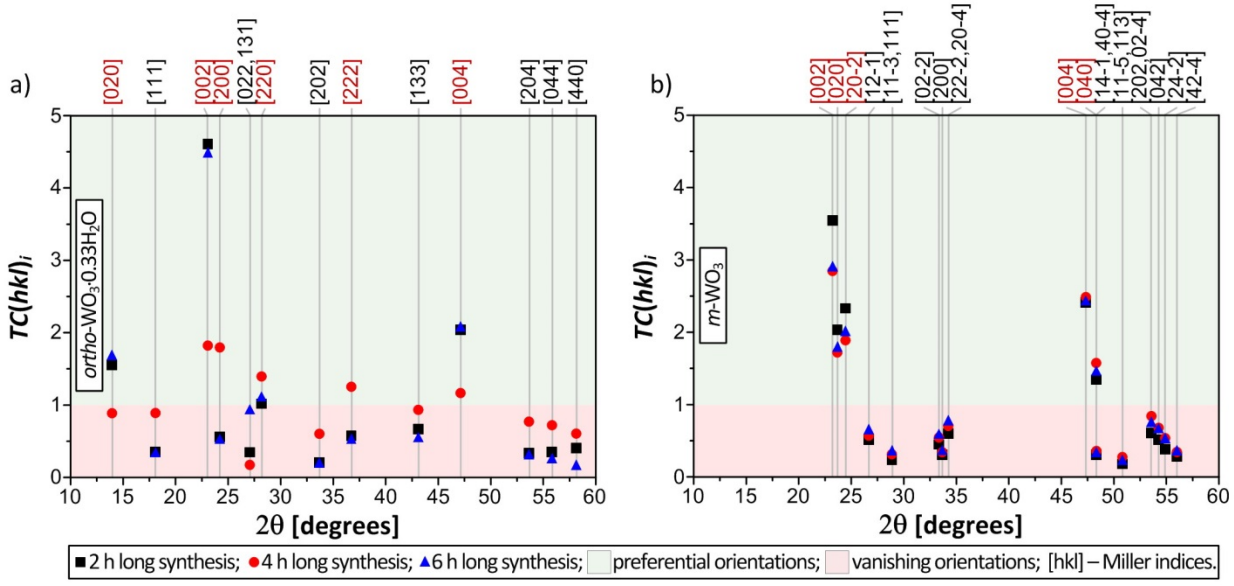

Figure S16. Texture coefficient spectra calculated for nanopowders obtained via hydrothermal syntheses performed from precursor dissolved in a) 0.3 M HCl and b) 3 M HCl, after 2 h, 4 h and 6 h;

An important input for 3D model creation of NPs, namely, shape, relative plane distances and estimation of interplanar angles were obtained from SEM micrographs (see Figure S17 and Figure 3 a - i in paper).

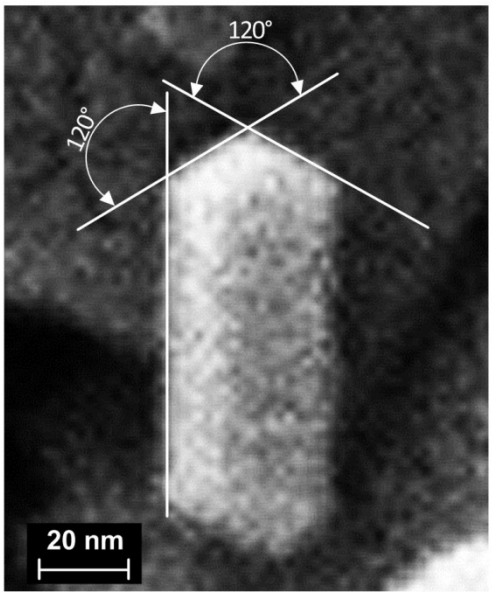

Figure S17. SEM image of a single *ortho*-$WO_3 \cdot 0.33H_2O$ NP obtained via hydrothermal synthesis performed from precursor dissolved in 0.3 M HCl after 6 h; white lines were drawn along the edges of the walls in order to estimate values of interplanar angles.

12. Fourier Transform Infrared Spectroscopy

The recorded FTIR spectra of obtained nanopowders presented in Figure S18 were studied in order to identify coordinated water molecules in $WO_5(H_2O)$ octahedron and vibrations in WO_6 octahedron in accordance to the state of the art.[6] The broad absorption band at 3470 cm^{-1} (-OH stretching) and sharp band at 1610 cm^{-1} (-OH in plane bending) have been observed in the powder synthesized from non-acetified precursor and precursor dissolved in 0.3 M HCl indicating high amount of water molecules in the powder. No indicators of water have been detected in the powder synthesized from the precursor dissolved in 3 M HCl indicating its anhydrous nature. The same samples exhibit also strong absorption band at 970 cm^{-1} and 1000 cm^{-1} corresponding to the W-O stretching in WO_6 octahedron. The broad band between 640 cm^{-1} and 955 cm^{-1} observed in all analyzed samples has been assigned to the W-O-W triplet stretching.

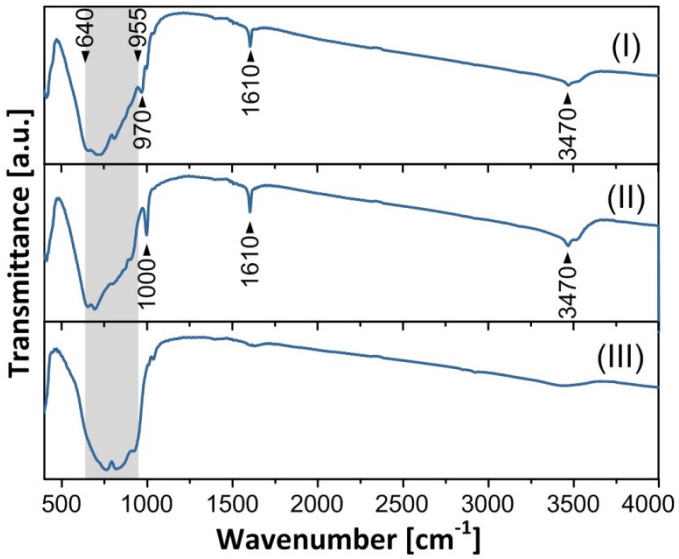

Figure S18. FTIR transmittance spectra of nanostructured products obtained from (I) non-acetified precursor solution, (II) precursor dissolved in 0.3 M HCl and (III) precursor dissolved in 3 M HCl after 6 h of hydrothermal synthesis.

13. Simultaneous Thermal Analysis (TG–DSC)

Thermal analysis was performed in order to determine the coordinated water content in a crystalline product of synthesis and to assess its thermal decomposition behavior.

The TG spectra presented in Figure S19 show distinct responses to increasing temperature in air atmosphere. The total weight loss observed up to 600 °C for NPs produced from non-acetified 0.3 M HCl and 3 M HCl precursor was 2.37 wt% (*m*-WO_3/*ortho*-$WO_3 \cdot 0.33H_2O$), 4.1 wt% (*ortho*-$WO_3 \cdot 0.33H_2O$) and 0.5 wt% (*m*-WO_3), respectively. The weight loss of *ortho*-$WO_3 \cdot 0.33H_2O$ is almost double of theoretically calculated value of 2.58% for structurally coordinated water. Higher value suggests the influence of physisorbed water on total weight loss, which can be confirmed by weight loss observation even below 100 °C.

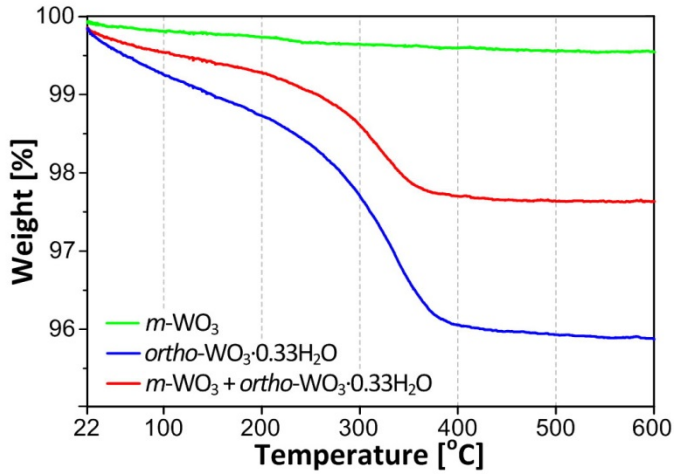

Figure S19. TG spectra of nanostructured products obtained from non-acetified precursor solution, precursor dissolved in 0.3 M and precursor dissolved in 3 M HCl after 6 h of hydrothermal synthesis.

The DSC curves (Figure S20) of NPs produced from non-acetified and 0.3 M HCl precursor exhibit sharp exothermic peak at 315 and 325 °C which correspond to removal of structurally coordinated water and formation of crystalline WO_3. No peaks were detected in DSC spectra of the dehydrated *m*-WO_3 synthesized from 3 M HCl precursor confirming the water absence suggested by FTIR data.

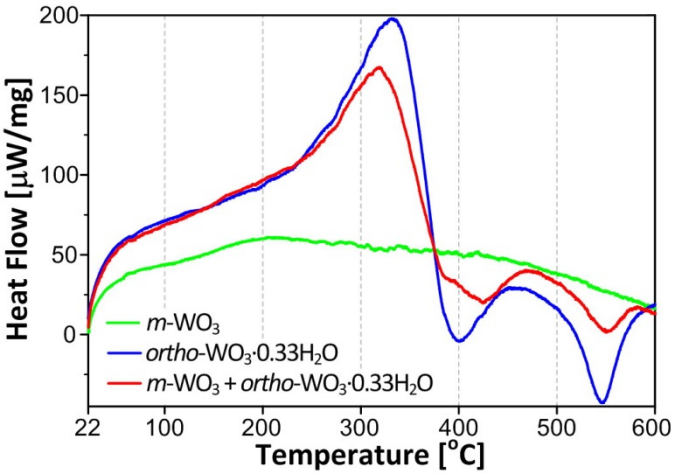

Figure S20. DSC spectra of nanostructured products obtained from non-acetified precursor solution, precursor dissolved in 0.3 M and precursor dissolved in 3 M HCl after 6 h of hydrothermal synthesis.

14. Model of agglomeration for various regular shaped NPs

An unfavorable aspect associated with nanostructured MO_X is the particles agglomeration leading to the formation of massive block, significantly reducing specific surface area. It is then important to access thoroughly the influence of NPs agglomeration and NPs size distribution on surface-to-volume ratio (SA:V). The simulated relations between SA:V and number of agglomerated particles are presented in Figure S21, where NPs of a few various shapes are described with simple assumption that the volume of all individual particles is equal. Particles presented in such simulation have primary and regular shapes with unit volume. However, it is very rare in practice to synthesize such ideal shaped nanostructures.

When considering the ideal dispersion of NPs in which agglomeration does not occur, nanoplates and nanodiscs are the most preferable in terms of SA:V value. For agglomerated NPs, higher values of SA:V are obtained for agglomerates of nanorods (agglomerates consisting of more than 3 NPs), although their individual specific surface area is not the highest among shapes under consideration. The least favorable seem to be nanocubes in case of which SA:V is small for fine dispersions and significantly drops down with increased number of agglomerated particles. As it is very rare in practice to synthesize not agglomerated NPs, it is assumed that 1D nanorods are the most desirable products of synthesis as long as their electrochemical application is concerned. In contrast to the agglomerated NPs, hollow and hierarchical nanostructures assembled in a highly periodic and porous manner generally exhibit much higher SA:V.[11,12] The van der Waals attraction between hierarchical structures is relatively weak due to larger size, which makes them more advantageous in dispersions when comparing to anisotropic NPs. However, the large size of such particles restricts their application in printable dispersions. The synthesis of highly porous, hierarchical MO_X nanostructures with sub-micrometer dimensions, although very promising, is still a challenging issue.

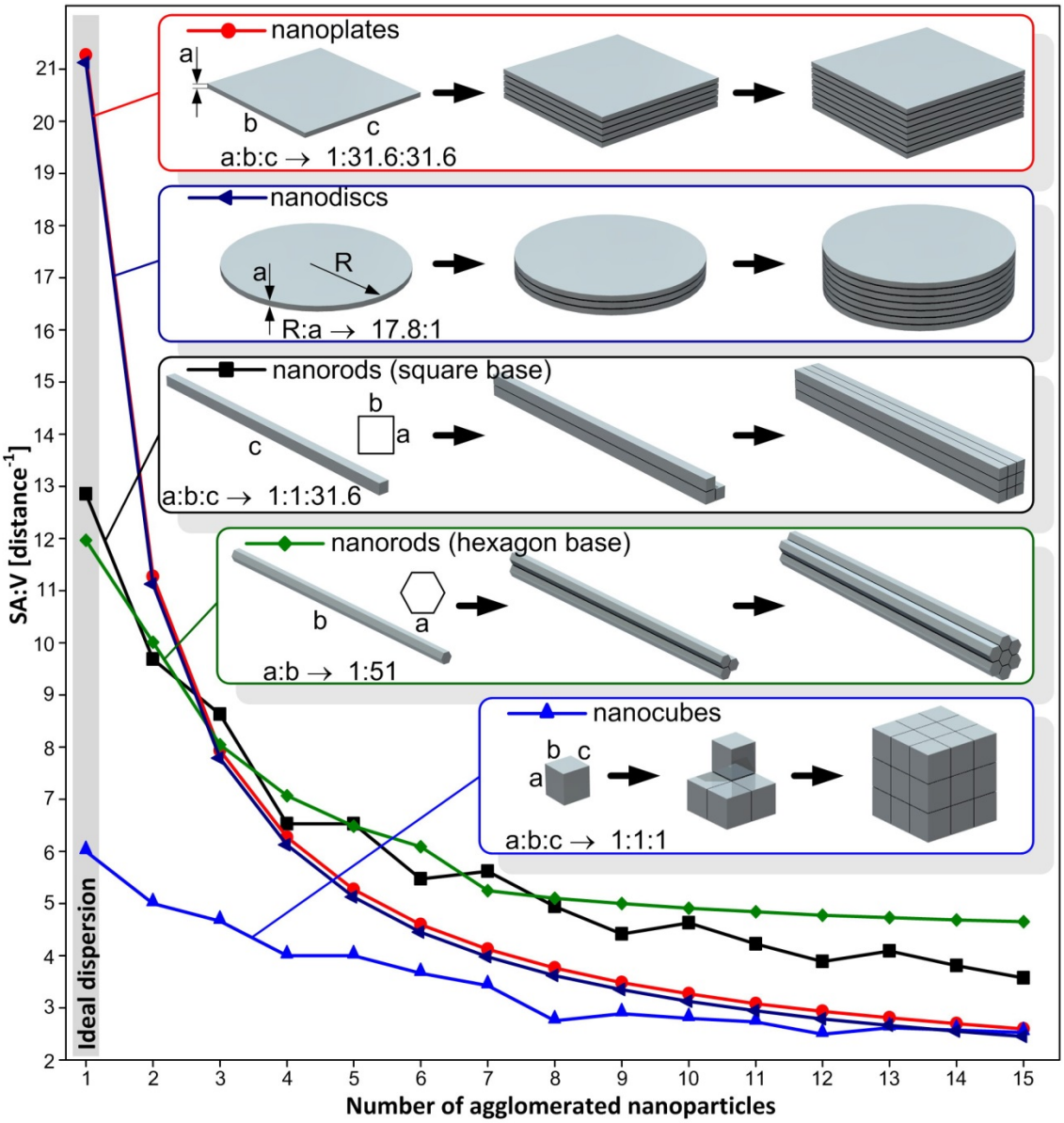

Figure S21. Model of agglomeration for various regular shaped NPs; the volume of all individual particles is equal to 1; the term 'ideal dispersion' refers to the situation in which agglomeration does not occur

15. Influence of the film thickness on electrochemical response

Influence of the film thickness on ΔOD shown in Figure S22 was measured for films with similar composition to the one reported in the present paper. In order to formulate an ink, 0.75 g of PTA was dissolved in 7.5 g of aqueous isopropyl alcohol mixture with weight ratio of 70:30 and

addition of oxalic acid in amount of 0.45 g. The solution was stirred for 15 minutes, 150 rpm at 60 °C and filtered (Roth, 0.45 μm syringe filter). Individual layers (1 cm^2) were printed 1, 3 and 5 times under equal environmental conditions on top of ITO PET substrate (Sigma-Aldrich, 1000 Å of ITO, 60 Ω/sq, T > 75 % at 550 nm). All films were dried at room temperature for 24 h and annealed in air at 120 °C (EHRET, TK4067, Germany) for 1 h. Detailed information on device encapsulation, experimental setup and measurements procedure can be found in our previous paper concerning dual-phase inkjet printed films.[13] Every successive printing pass causes the layer grow of about 23 nm. Films printed 5 times exhibit change in optical density almost twice higher than films printed with single pass.

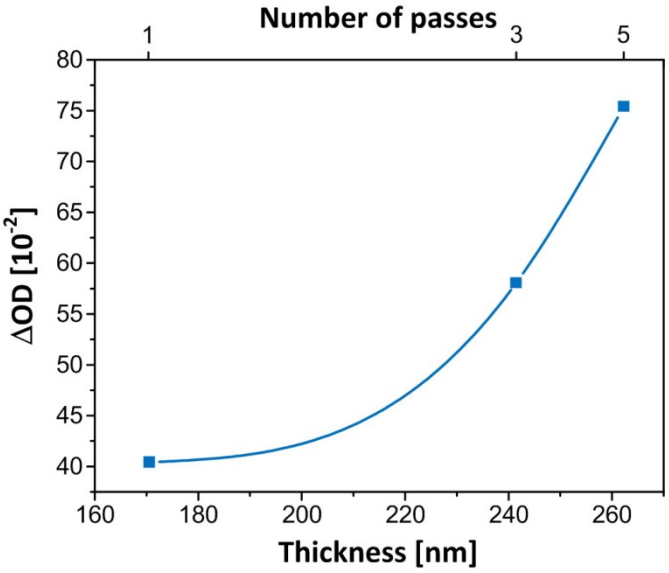

Figure S22. Change in optical density in function of the *a*-WO_3 film thickness. The EC action was induced by applying voltage of ±4V.

16. Spectral response

Transmittance spectra for dual-phase films containing NPs synthesized in 6 h long process under various precursor acidities in their colored and bleached states are illustrated in Figure S23. In the bleached state all samples have high transmittances in a visible region indicating high transparency of the coatings. Under application of a negative voltage (-2 V), all microstructures exhibited observable transmittance modulation performance. The apparent transmittance reduction of *a*-WO_3/(*m*-WO_3 + *ortho*-$WO_3 \cdot 0.33H_2O$) at ~525 nm comes from the existence of both crystalline phases.

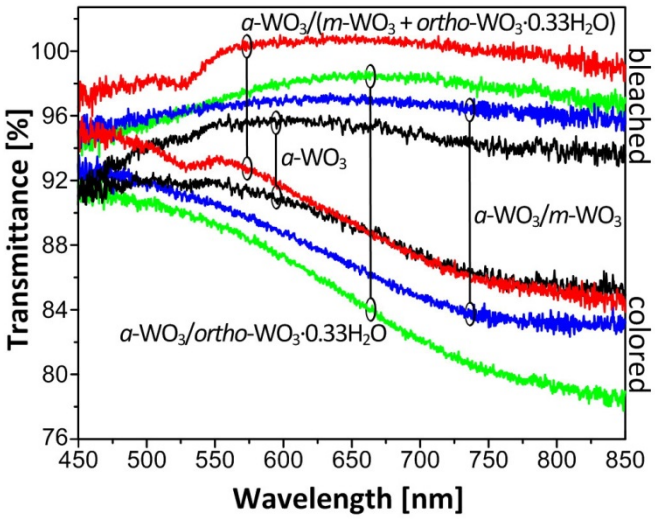

Figure S23. UV-vis transmittance of dual-phase inkjet printed films containing NPs synthesized in 6 h long process under various precursor acidities; bleaching and coloring optical states were induced by ±2 V operational voltages.

17. Graphics

Graphical processing of scientific recults concerning: graphical methods in measurments, photo processing, vector image processing, arrangement of curvers and subfigures, and file formating was performed according to video tutorials published in KEEP CALM and PUBLISH PAPERS blog: http://www.keepcalmandpublishpapers.com

This source of knowledge contains a number of short (<15 min) video tutorials concerning preparation of graphics for scientific communications. Each tutorial sets out a clear strategy to assist students and researchers in creating effective visual graphics for journal submissions, grant proposals, theses, posters and presentations. Each video tutorial is accompanied with written post which gives an introduction to presented methods and techniques.

References

1. J. J. Cooper-White, J. E. Fagan, V. Tirtaatmadja, D. R. Lester, and D. V. Boger, *J. Nonnewton. Fluid Mech.*, 2002, **106**, 29–59.

2. R. J. Furbank and J. F. Morris, *Phys. Fluids*, 2004, **16**, 1777.

3. T. R. Tuladhar and M. R. Mackley, *J. Nonnewton. Fluid Mech.*, 2008, **148**, 97–108.

4. M. Denesuk and D. R. Uhlmann, *J. Electrochem. Soc.*, 1996, **143**, L186–L188.

5. S. Ruppi, *Int. J. Refract. Met. Hard Mater.*, 2005, **23**, 306–316.

6. J. Pfeifer, C. Guifang, P. Tekula-Buxbaum, B. A. Kiss, M. Frakas-Jahnke, and K. Vadasdi, *J. Solid State Chem.*, 1995, **119**, 90–97.

7. J. Jiang, Y. Li, J. Liu, X. Huang, C. Yuan, and X. W. D. Lou, *Adv. Mater.*, 2012, **24**, 5166–80.

8. P. M. Woodward, A. W. Sleight, and T. Vogt, *J. Solid State Chem.*, 1997, **131**, 9–17.

9. K. Yamanaka, H. Oakamoto, H. Kidou, and T. Kudo, *Jpn. J. Appl. Phys.*, 1986, **25**, 1420–1426.

10. M. Law, L. E. Greene, J. C. Johnson, R. Saykally, and P. Yang, *Nat. Mater.*, 2005, **4**, 455–9.

11. J.-H. Lee, *Sensors Actuators B Chem.*, 2009, **140**, 319–336.

12. Z. Gu, T. Zhai, B. Gao, X. Sheng, Y. Wang, and H. Fu, *J. Phys. Chem. B*, 2006, **110**, 23829–23836.

13. P. J. Wojcik, A. S. Cruz, L. Santos, L. Pereira, R. Martins, and E. Fortunato, *J. Mater. Chem.*, 2012, **22**, 13268.